

Beyond Performance/Cost Tradeoffs in Motion Control: A Multirate Feedforward Design With Application to a Dual-Stage Wafer System

Jurgen van Zundert¹, Tom Oomen¹, *Senior Member, IEEE*, Jan Verhaegh, Wouter Aangenent, Duarte J. Antunes², *Member, IEEE*, and W. P. M. H. Heemels¹, *Fellow, IEEE*

Abstract—Motion systems with multiple control loops often run at a single sampling rate for simplicity of implementation and controller design. The achievable performance in terms of position accuracy is determined by the data acquisition hardware, such as sensors, actuators, and analog-to-digital/digital-to-analog converters, which is typically limited due to economic cost considerations. The aim of this paper is to develop a multirate approach to go beyond this traditional performance/cost tradeoff, i.e., to use different sampling rates in different control loops to optimally use hardware resources. The approach appropriately deals with the inherent time-varying behavior that is introduced by multirate sampling. A multirate feedforward control design framework is presented to optimize the tracking of a dual-stage multirate system. The application of the proposed approach to an industrial dual-stage wafer system demonstrates the advantages of multirate control, both in simulations and experiments.

Index Terms—Dual-stage system, experiments, feedforward design, multirate control, performance/cost tradeoff, wafer stage application.

I. INTRODUCTION

MULTIVARIABLE control systems, including those in motion systems, are often implemented digitally since it offers flexibility and directly connects to the digital supervisory layers. The digital implementation requires analog-to-digital and digital-to-analog conversion. For motion systems, these processes are often executed using fixed, single-rate sampling schemes [1], [2], i.e., homogeneous for all loops, since for linear time-invariant (LTI) systems it enables controller design using well-developed design approaches. In particular, it allows the use of frequency-domain techniques such as Bode

plots and Nyquist diagrams [3], which find application in various areas of controller design, including feedback control [3], [4], feedforward control [5], and iterative learning control (ILC) [6].

Fixed, single-rate sampling is preferred from a controller design point of view, but not from a performance versus cost point of view. As an example, consider systems with multiple control loops, where only one limits the overall performance. The performance of a control loop can be increased by increasing the sampling frequency of that loop. For single-rate implementations, this implies that if the performance of one of the loops is increased, the sampling frequency of all loops needs to be increased. Obviously, such an approach is expensive in terms of the required hardware, such as sensors, actuators, and analog-to-digital/digital-to-analog converters, since all loops are affected while only one is limiting performance.

From a performance versus cost point of view, flexible sampling is preferred over fixed sampling (see also Fig. 1). Examples of flexible sampling include multirate control [7]–[16], sparse control [17], and nonequidistant sampling [18], [19]. Indeed, a multirate approach is more natural for multiloop systems with different performance requirements, but also for systems with different time scales such as thermomechanical systems [20]. Sparse control and nonequidistant sampling are used in, e.g., systems with limited resources and optimal resource allocation [18], [21].

Flexible sampling has a large potential, but its deployment is hampered by a lack of control design techniques. This is mainly caused by the fact that flexible sampling introduces time-varying behavior [1, Sec. 3.3]. In particular, a flexible sampling of an LTI system yields a linear periodically time-varying (LPTV) system. Due to the time variance, the frequency-domain control design techniques mentioned earlier are not (directly) applicable. Frequency-domain design for linear time-varying systems is investigated in [22]–[26] and linear time-varying feedforward design is investigated in [19] and [27], but at present, there is no systematic control design framework available.

Although flexible sampling has the potential to go beyond the traditional performance/cost tradeoff for fixed sampling, as shown in Fig. 1, at present, its deployment is hampered by a lack of control design techniques for such sampling schemes. In this paper, a framework to exploit multirate feedforward

Manuscript received February 5, 2018; revised August 21, 2018; accepted October 21, 2018. Date of publication December 13, 2018; date of current version February 14, 2020. Manuscript received in final form November 13, 2018. This work was supported by the Netherlands Organisation for Scientific Research through research programmes Robust Cyber-Physical Systems under Grant 12694 and VIDI under Grant 15698. Recommended by Associate Editor C. Manzie. (Corresponding author: Jurgen van Zundert.)

J. van Zundert, T. Oomen, J. Verhaegh, D. J. Antunes, and W. P. M. H. Heemels are with the Department of Mechanical Engineering, Control Systems Technology Group, Eindhoven University of Technology, 5612 AZ Eindhoven, The Netherlands (e-mail: j.c.d.v.zundert@tue.nl; t.a.e.oomen@tue.nl; jan.verhaegh@tuo.nl; d.antunes@tue.nl; w.p.m.h.heemels@tue.nl).

W. Aangenent is with ASML Research Mechatronics and Control, 5504 DR Veldhoven, The Netherlands (e-mail: wouter.aangenent@asml.com).

Color versions of one or more of the figures in this article are available online at <http://ieeexplore.ieee.org>.

Digital Object Identifier 10.1109/TCST.2018.2882341

1063-6536 © 2018 IEEE. Personal use is permitted, but republication/redistribution requires IEEE permission.

See <https://www.ieee.org/publications/rights/index.html> for more information.

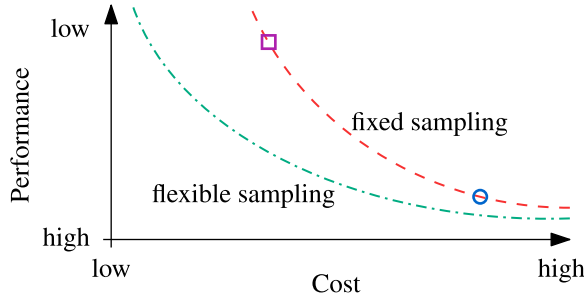


Fig. 1. Low sampling frequency is inexpensive in terms of implementation cost, but yields low performance (□). A high sampling frequency yields high performance, but is expensive (○). This performance/cost tradeoff is inherent to traditional fixed sampling (---). Flexible sampling goes beyond this tradeoff through use of different sampling frequencies in different control loops. Essentially, the performance/cost tradeoff can be decided upon per control loop, resulting in an improved overall tradeoff (-.-.-).

controller design is presented to overcome this restriction, and thereby go beyond the traditional performance/cost tradeoff. Application of the framework focuses on precision motion systems. In particular, the framework is demonstrated on an experimental dual-stage system, as standard in, e.g., wafer stages [28, Ch. 9].

The main contribution of this paper is a framework to exploit multirate control for performance improvement. The following subcontributions are identified: 1) multirate controller design based on multirate system descriptions, including time variance; 2) controller optimization addressing nonperfect models; 3) performance improvement by exploiting time variance; 4) application of the design framework in simulation; and 5) experimental validation on a dual-stage system.

Initial results on simulation level can be found in [29] and related work on minimizing intersample behavior in digital control systems can be found in [1], [25], and [30]. This paper contains substantial original contributions including Contribution (I), Contribution (II), and Contribution (V). Related work on wafer stage control design includes feedback control [31], [32], feedforward control [33], linear parameter varying control [34], and sparse control [17]. In this paper, previously unexplored freedom in sampling is exploited, which makes the approach complementary to other approaches.

This paper is organized as follows. In Section II, the main problem that is considered to improve the performance/cost tradeoff through multirate control is presented. In Section III, the multirate control system is modeled. The multirate controller design is presented in Section IV. Furthermore, the performance is further improved by exploiting properties of time-varying systems. The controller design is applied to an experimental setup resembling a dual-stage wafer system. The experimental setup is detailed in Section V. Simulation results are presented in Section VI and experimental results are presented in Section VII. Conclusions are given in Section VIII.

II. PROBLEM DEFINITION

In this paper, a framework is presented to enhance the performance/cost tradeoff through multirate control. In this section, the main problem is presented.

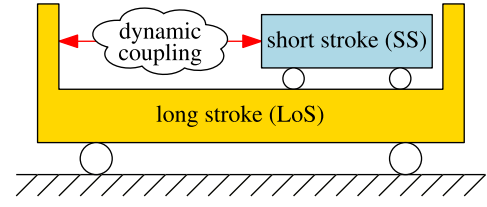


Fig. 2. Dual-stage systems consist of two subsystems: a short stroke for high precision and a long stroke to cover large ranges. The combined system provides high positioning accuracy over a large range.

A. Application Motivation—Dual-Stage Motion Systems With Large Differences in Performance Requirements

In many motion control applications, a high positioning accuracy is required over a large range. For such systems, a single-stage design may not suffice due to the large dynamic range. To achieve high precision over a large range, a dual-stage system can be used.

A dual-stage system, as illustrated in Fig. 2, consists of two subsystems: a short stroke (SS) with a high positioning accuracy (and limited range) connected to a long stroke (LoS) with a large range (and limited positioning accuracy). If designed properly, the dual-stage system is able to cover a large range with high positioning accuracy. Clearly, there is a large difference between the performance requirements of the two subsystems.

An example of a dual-stage system is a wafer stage in lithography machines [28, Ch. 9]. Wafer stages require an accuracy up to nanometer level over a range of 1 m ([35], [28, Sec. 9.3.1]), resulting in a large dynamic range of $\mathcal{O}(10^9)$. Therefore, wafer stages are typically constructed as dual-stage systems. More details on the wafer stage application are presented in Section V.

B. Performance/Cost Perspective on Multivariable Systems With Large Differences in Performance Requirements

In view of the performance/cost tradeoff in Fig. 1, different (control) requirements for the subsystems of the dual-stage design provide an excellent opportunity to exploit multirate control to go beyond performance/cost tradeoffs in motion control.

The considered multirate control architecture is shown in Fig. 3 where a high sampling frequency f_h is used for the short stroke $G_{SS,h}$ in Fig. 1) and a low sampling frequency f_l is used for the long stroke $G_{LoS,l}$ to reduce cost in Fig. 1). The short-stroke system $G_{SS,h}$ tracks reference trajectory $p_{SS,h}$. The long-stroke system $G_{LoS,l}$ tracks the position of $G_{SS,h}$ to ensure the short stroke is within range and reaction forces are limited. The downsampler \mathcal{D}_F facilitates the sampling rate conversion. The control design of both subsystems consists of feedback control (C_{FB}), feedforward control (C_{FF}), and input shaping (C_ψ).

For design of the long-stroke controllers, the interest is in the position error between the two stages during exposure, i.e., during the scanning motion, to limit reaction forces to the short stroke. This error measured at the highest possible sampling frequency f_* is denoted ε_* and not available for real-time control, but typically available afterward for performance

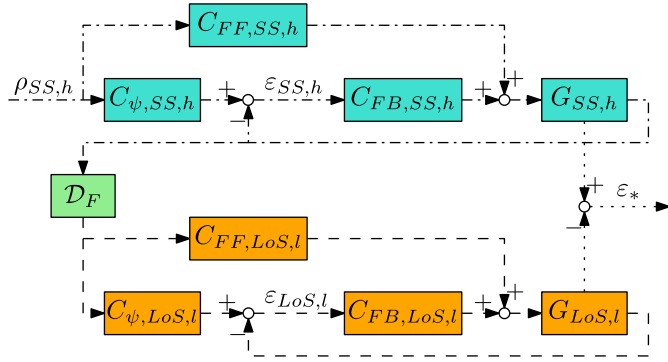


Fig. 3. Multirate control configuration for a dual-stage system. The top part relates to the short stroke at high-rate f_h . The bottom part relates to the long stroke at low rate f_l . The long stroke tracks the output position of the short stroke, where downsampler \mathcal{D}_F facilitates the sampling rate conversion. Dotted lines: extreme high sampling rates f_* . Dashed-dotted lines: high sampling rates f_h . Dashed lines: low sampling rates f_l . Both control loops include a feedback controller C_{FB} , a feedforward controller C_{FF} , and an input shaper C_ψ . The objective is to minimize position difference ε_* through design of $C_{\psi,LoS,l}$ and $C_{FF,LoS,l}$.

evaluation. The sampling frequencies are related by

$$f_* = F_h f_h = F_l f_l, \quad f_h = F f_l \quad (1)$$

where $F_l \geq F_h \geq 1$, $F := (F_l/F_h)$, with $F_h, F_l, F \in \mathbb{N}$. In this paper, finite-time signals are considered of which the signal lengths are related as

$$N_* = F_h N_h = F_l N_l, \quad N_h = F N_l \quad (2)$$

as directly follows from (1).

Remark 1: The assumption of integer sampling rate factors in (1) is imposed for ease of notation, but can easily be relaxed if the factor is a rational number. The proposed approach is not applicable for irrational factors, although these can often be closely approximated with rational factors.

C. Problem Formulation—Framework for Exploiting Multirate Sampling for Enhanced Control Performance

In this paper, the following problem is considered.

Main Problem: Given the multirate control configuration in Fig. 3 with sampling frequencies admitting (1), a given finite-time reference trajectory $\rho_{SS,h} \in \mathbb{R}^{N_h}$ for $\rho_{SS,h}$, models $G_{SS,*}$, $G_{LoS,*}$ of $G_{SS,h}$, $G_{LoS,l}$ at sampling frequency f_* , and controllers $C_{FF,SS,h}$, $C_{\psi,SS,h}$, $C_{FB,SS,h}$, $C_{FF,LoS,l}$, determine

$$(C_{FF,LoS,l}, C_{\psi,LoS,l}) = \arg \min_{C_{FF,LoS,l}, C_{\psi,LoS,l}} \|\varepsilon_*\|_2^2 \quad (3)$$

where $\varepsilon_* \in \mathbb{R}^{N_*}$ denotes the position error ε_* over the considered interval.

Controllers $C_{FF,SS,h}$, $C_{\psi,SS,h}$, and $C_{FB,SS,h}$ are often available from earlier control designs based on the single-rate short-stroke system only, neglecting the long-stroke system and multirate aspects. A similar reasoning holds for $C_{FF,LoS,l}$. It is assumed that $C_{FB,SS,h}$ and $C_{FB,LoS,l}$ stabilize the short-stroke and long-stroke system, respectively. Note that stability is not affected by $C_{FF,LoS,l}$, $C_{\psi,LoS,l}$.

Importantly, control objective (3) incorporates the dynamics of the short stroke for design of the long-stroke controllers

$C_{FF,LoS,l}$, $C_{\psi,LoS,l}$. Moreover, it considers ε_* rather than $\varepsilon_{LoS,l}$ and thereby takes intersample behavior into account, which is an important aspect in multirate control [25]. Note that (3) is posed in terms of finite-time signals, rather than infinite-time signals, since, in practice, tasks have a finite length.

The presented framework allows to recover single-rate control as a special case of multirate control by setting $F_h = F_l$. In Sections VI and VII, multirate control is compared with single-rate control.

D. Notation

Matrix variables are underlined, with \underline{I}_n the $n \times n$ identity matrix, $\underline{0}_{m \times n}$ the $m \times n$ zero matrix, $\underline{1}_n$ the $n \times 1$ ones vector with all elements 1, and \underline{e}_n the $n \times 1$ unit vector with the first element 1 and others 0. Vector $\underline{\alpha} \in \mathbb{R}^N$, $N \in \mathbb{N}$, is given by $\underline{\alpha} = [\alpha[0] \ \alpha[1] \ \dots \ \alpha[N-1]]^\top$, with transpose $(\cdot)^\top$ and $\|\underline{\alpha}\|_2^2 = \underline{\alpha}^\top \underline{\alpha}$. The Kronecker product is denoted \otimes and $\text{diag}\{\cdot\}$ denotes a diagonal matrix with diagonal entries (\cdot) . The floor operator is given by $\lfloor x \rfloor = \max\{m \in \mathbb{Z} \mid m \leq x\}$. The discrete-time delay operator is denoted as z^{-1} .

III. MULTIRATE CONTROL SYSTEM

In this section, the model-based multirate controller design is presented, which constitutes Contribution (I). In Section III-A, the time-varying aspects of multirate systems are modeled. In Section III-B, these models are used to describe the multirate control diagram in Fig. 3. Based on these results, the multirate controller is presented in Section IV.

A. Modeling Multirate Systems—Time-Varying Aspects

In this section, building blocks to model the multirate system in Fig. 3 are presented. The system is modeled over the finite-time length considered in the main problem in Section II-C.

Consider a causal, single-input, single-output, discrete-time, LTI system H with Markov parameters $h(k) \in \mathbb{R}$, $k = 0, 1, \dots, N-1$. The mapping from the finite-time input $\underline{\alpha} \in \mathbb{R}^N$ to the finite-time output $\underline{\beta} \in \mathbb{R}^N$ is given by $\underline{H} \in \mathbb{R}^{N \times N}$ via

$$\underline{\beta} = \underline{H} \underline{\alpha}, \quad (4)$$

$$\begin{bmatrix} \beta[0] \\ \beta[1] \\ \beta[2] \\ \vdots \\ \beta[N-1] \end{bmatrix} = \begin{bmatrix} h(0) & 0 & 0 & \dots & 0 \\ h(1) & h(0) & 0 & \dots & 0 \\ h(2) & h(1) & h(0) & \dots & 0 \\ \vdots & \vdots & \vdots & \ddots & \vdots \\ h(N-1) & h(N-2) & h(N-3) & \dots & h(0) \end{bmatrix} \times \begin{bmatrix} \alpha[0] \\ \alpha[1] \\ \alpha[2] \\ \vdots \\ \alpha[N-1] \end{bmatrix}. \quad (5)$$

Since $\underline{\alpha}, \underline{\beta}$ have the same sampling frequency, \underline{H} is square. Moreover, since H is causal and time-invariant, \underline{H} is lower triangular and Toeplitz, respectively [1].

The multirate system in Fig. 3 involves different sampling frequencies. The conversions between different sampling frequencies are given as follows (see also [36, Sec. 4.1.1] and [25, Definition 5]). Let $\underline{\alpha} \in \mathbb{R}^{FN}$, $F, N \in \mathbb{N}$, then the downsampling operator $\mathcal{D}_F : \mathbb{R}^{FN} \mapsto \mathbb{R}^N$ with factor F yields $\underline{\beta} = \mathcal{D}_F(\underline{\alpha}) \in \mathbb{R}^N$ where

$$\beta[k] = \alpha[Fk], \quad k = 0, 1, \dots, N-1. \quad (6)$$

Let $\underline{\alpha} \in \mathbb{R}^N$, $N \in \mathbb{N}$, then the upsampling operator $\mathcal{S}_{u,F} : \mathbb{R}^N \mapsto \mathbb{R}^{FN}$ with factor $F \in \mathbb{N}$ yields $\underline{\beta} = \mathcal{S}_{u,F}(\underline{\alpha}) \in \mathbb{R}^{FN}$ where

$$\beta[k] = \begin{cases} \alpha\left[\frac{k}{F}\right], & k = 0, F, 2F, \dots, (N-1)F \\ 0, & \text{otherwise.} \end{cases} \quad (7)$$

The upsampling operator inserts zeros in between the values of the low-rate signal to create a high-rate signal. The interpolation is performed using a zero-order-hold interpolator. In terms of discrete-time transfer functions, the zero-order-hold interpolator with factor $F \in \mathbb{N}$ is defined as

$$\mathcal{I}_{\text{ZOH},F} = \sum_{f=0}^{F-1} z^{-f}. \quad (8)$$

The zero-order-hold interpolator is used in combination with the upsampling operator for upsampling. The resulting zero-order-hold upsampler is defined by $\mathcal{H}_F := \mathcal{I}_{\text{ZOH},F} \mathcal{S}_{u,F}$, i.e., let $\underline{\alpha} \in \mathbb{R}^N$, $N \in \mathbb{N}$, then \mathcal{H}_F with factor $F \in \mathbb{N}$ yields $\underline{\beta} = \mathcal{H}_F(\underline{\alpha}) \in \mathbb{R}^{FN}$ where

$$\beta[k] = \alpha\left[\left\lfloor \frac{k}{F} \right\rfloor\right], \quad k = 0, 1, \dots, (N-1)F. \quad (9)$$

The system description and controller design are based on finite-time descriptions. The finite-time description of the downsampling operator \mathcal{D}_F with factor $F \in \mathbb{N}$ is given by

$$\underline{\mathcal{D}}_F = \underline{I}_N \otimes \underline{e}_F^\top \in \mathbb{R}^{N \times FN} \quad (10)$$

i.e., let $\underline{\alpha} \in \mathbb{R}^{FN}$, $N \in \mathbb{N}$ and let $\underline{\beta} \in \mathbb{R}^N$ be given by (6), then $\underline{\beta} = \underline{\mathcal{D}}_F \underline{\alpha}$ with $\underline{\mathcal{D}}_F$ in (10). The finite-time description of the zero-order-hold upsampling operator \mathcal{H}_F with factor $F \in \mathbb{N}$ is given by

$$\underline{\mathcal{H}}_F = \underline{I}_N \otimes \underline{1}_F \in \mathbb{R}^{FN \times N} \quad (11)$$

i.e., let $\underline{\alpha} \in \mathbb{R}^N$, $N \in \mathbb{N}$ and let $\underline{\beta} \in \mathbb{R}^{FN}$ be given by (9), then $\underline{\beta} = \underline{\mathcal{H}}_F \underline{\alpha}$ with $\underline{\mathcal{H}}_F$ in (11). Examples of $\underline{\mathcal{D}}_F$ and $\underline{\mathcal{H}}_F$ are provided in Example 2.

Example 2 (Downsampler and Upsampler): Let $F = 2$, $N = 3$, then $\underline{\mathcal{D}}_F$ in (10) and $\underline{\mathcal{H}}_F$ in (11) are given by

$$\underline{\mathcal{D}}_F = \begin{bmatrix} 1 & 0 & 0 & 0 & 0 & 0 \\ 0 & 0 & 1 & 0 & 0 & 0 \\ 0 & 0 & 0 & 0 & 1 & 0 \end{bmatrix}, \quad \underline{\mathcal{H}}_F = \begin{bmatrix} 1 & 0 & 0 \\ 1 & 0 & 0 \\ 0 & 1 & 0 \\ 0 & 1 & 0 \\ 0 & 0 & 1 \\ 0 & 0 & 1 \end{bmatrix}. \quad (12)$$

Let $\underline{\alpha} = [1 \ 2 \ 3 \ 4 \ 5 \ 6]^\top$, then $\underline{\beta} := \mathcal{D}_F(\underline{\alpha}) = \underline{\mathcal{D}}_F \underline{\alpha} = [1 \ 3 \ 5]^\top$ and $\underline{\gamma} := \mathcal{H}_F(\underline{\beta}) = \underline{\mathcal{H}}_F \underline{\beta} = [1 \ 1 \ 3 \ 3 \ 5 \ 5]^\top$. Note that

$\underline{\gamma} = \underline{\mathcal{H}}_F \underline{\mathcal{D}}_F \underline{\alpha} \neq \underline{\alpha}$, since

$$\underline{\mathcal{H}}_F \underline{\mathcal{D}}_F = \begin{bmatrix} 1 & 0 & 0 & 0 & 0 & 0 \\ 1 & 0 & 0 & 0 & 0 & 0 \\ 0 & 0 & 1 & 0 & 0 & 0 \\ 0 & 0 & 1 & 0 & 0 & 0 \\ 0 & 0 & 0 & 0 & 1 & 0 \\ 0 & 0 & 0 & 0 & 1 & 0 \end{bmatrix} \neq \underline{I}_6. \quad (13)$$

Example 2 shows that down/up sampling affects the signal. More generally, using the Kronecker mixed-product property

$$(\underline{A} \otimes \underline{B})(\underline{C} \otimes \underline{D}) = (\underline{A}\underline{C}) \otimes (\underline{B}\underline{D}) \quad (14)$$

it can be shown that

$$\underline{\mathcal{D}}_F \underline{\mathcal{H}}_F = \underline{I}_N, \quad \underline{\mathcal{H}}_F \underline{\mathcal{D}}_F = \underline{I}_N \otimes (\underline{1}_F \underline{e}_F^\top) \neq \underline{I}_{FN}. \quad (15)$$

A key observation is that up/down sampling $\underline{\mathcal{D}}_F \underline{\mathcal{H}}_F$ has no effect on the signal, whereas down/up sampling $\underline{\mathcal{H}}_F \underline{\mathcal{D}}_F$ does affect the signal. In fact, $\underline{\mathcal{H}}_F \underline{\mathcal{D}}_F$ is block Toeplitz with block size F , see also Example 2, and hence the down/up sampling operation is not LTI, but LPTV with period F . An important consequence is that if an input-output operation involves any sampling rate lower than the input sampling rate, then the operation is LPTV. Indeed, this is the case for the multirate control diagram in Fig. 3, which is thus LPTV. The presented finite-time descriptions enable to exactly describe this time-varying multirate system.

In Section III-B, the multirate control diagram is presented, based on the finite-time descriptions presented in this section.

Remark 3: A more general definition of the downsampler \mathcal{D}_F in (6) is obtained by considering $\alpha \in \mathbb{R}^M$, $\beta \in \mathbb{R}^{\lceil (M/F) \rceil}$, $F, M \in \mathbb{N}$. For ease of notation, it is assumed that $M = FN$.

B. Multirate Control Diagram

The full control diagram of the architecture in Fig. 3 is shown in Fig. 4 and includes the modeling of systems $G_{\text{SS},h}$ and $G_{\text{LoS},l}$. The systems are modeled through $G_{\text{SS},*}$ and $G_{\text{LoS},*}$ operating at the extremely high-rate f_* , which approximate the underlying continuous-time systems G_{SS} and G_{LoS} , respectively. Here, \mathcal{H}_* , \mathcal{S}_* are the continuous-time hold (digital-to-analog) and sampling (analog-to-digital converter). Recall that signals at rate f_* are not available for real-time feedback control. However, this approach enables the evaluation of the tracking error ε_* at rate f_* .

To determine the optimal controllers, the relation between $C_{\text{FF},\text{LoS},l}$, $C_{\psi,\text{LoS},l}$, and ε_* is required. The dependence of finite-time $\underline{\varepsilon}_*$ on $\underline{\rho}_{\text{SS},h}$, $\underline{\nu}_{\text{FF},\text{LoS},l}$, $\underline{\rho}_{\psi,\text{LoS},l}$ is given by Lemma 4.

Lemma 4: Given the finite-time descriptions in Section III-A, $\underline{\varepsilon}_*$ in Fig. 4 is given by

$$\underline{\varepsilon}_* = \underline{\psi}_{\text{SS},*} - \underline{A} \begin{bmatrix} \underline{\nu}_{\text{FF},\text{LoS},l} \\ \underline{\rho}_{\psi,\text{LoS},l} \end{bmatrix} \quad (16)$$

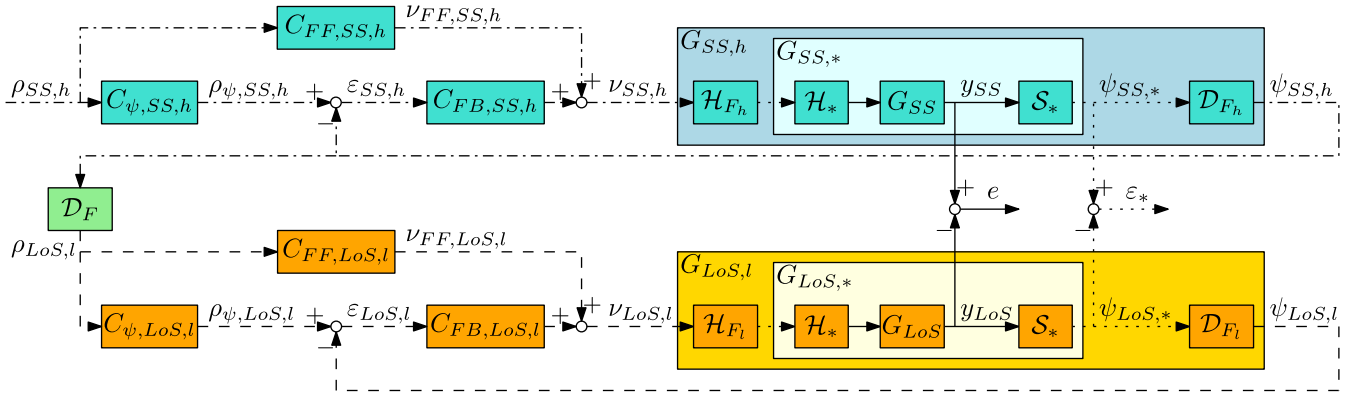


Fig. 4. Multirate control architecture where the short-stroke loop (top) runs at high rate f_h and the long-stroke loop (bottom) at low rate f_l . The interconnection is provided through downsampler \mathcal{D}_F . Error e_* is an approximation of the continuous-time signal e at extreme high-rate f_* . Solid lines: continuous-time signals. Dotted lines: extreme high sampling rates f_* . Dashed-dotted lines: high sampling rates f_h . Dashed lines: low sampling rates f_l . Both subsystems (G) are controlled through feedback (C_{FB}), feedforward (C_{FF}), and input shaping (C_ψ). The objective is to minimize e_* through design of $C_{FF,LoS,l}$ and $C_{\psi,LoS,l}$ such that the long stroke tracks the short stroke. In this configuration, $C_{FF,LoS,l}$ and $C_{\psi,LoS,l}$ are implemented at the low rate, i.e., $f_c = f_l$.

with

$$\underline{\psi}_{SS,*} = \underline{G}_{SS,*} \underline{\mathcal{H}}_{F_h} \underline{\mathcal{S}}_{SS,h} \times (\underline{C}_{FF,SS,h} + \underline{C}_{FB,SS,h} \underline{C}_{\psi,SS,h}) \underline{\rho}_{SS,h} \quad (17)$$

$$\underline{\mathcal{A}} = \underline{G}_{LoS,*} \underline{\mathcal{H}}_{F_l} \underline{\mathcal{S}}_{LoS,l} [\underline{L}_{N_l} \underline{C}_{FB,LoS,l}] \quad (18)$$

$$\underline{\mathcal{S}}_{SS,h} = (\underline{L}_{N_h} + \underline{C}_{FB,SS,h} \underline{G}_{SS,h})^{-1} \quad (19)$$

$$\underline{\mathcal{S}}_{LoS,l} = (\underline{L}_{N_l} + \underline{C}_{FB,LoS,l} \underline{G}_{LoS,l})^{-1}. \quad (20)$$

Proof: See Appendix A. \square

An important observation in Lemma 4 is that $\underline{\mathcal{A}}$ includes sampling rate changes, and hence, the transfer function from $\underline{\nu}_{FF,LoS,l}$, $\underline{\rho}_{\psi,LoS,l}$ to \underline{e}_* is LPTV and cannot be described using traditional frequency-domain transfer functions. In Section IV, the controllers are designed.

IV. MULTIRATE CONTROLLER DESIGN

In Section III-B, the multirate system in Fig. 4 is modeled. In this section, the controllers are parameterized and the optimal controller parameters are presented, constituting Contribution (II). Furthermore, the multirate system is further improved by modifying the controller implementation and design, which constitutes Contribution (III).

A. Controller Parameterization

To address arbitrary reference trajectories, the feedforward and input shaping filters are parameterized in terms of basis functions (see [37], [38]). Basis functions decouple the parameters from the reference trajectory, allowing variations in the reference trajectories without affecting the parameters. This is in contrast to standard learning approaches [6] in which a command signal for one specific reference trajectory is learned.

Inspired by [39], controllers $C_{FF,LoS,l}$, $C_{\psi,LoS,l}$ are parameterized in terms of difference operators according to Definition 5. Note that $C_{FF,LoS,l}(0) = 0$ and $C_{\psi,LoS,l}(0) = 1$ such that if the parameters are zero, only feedback control is used.

Definition 5: $C_{FF,LoS,l}$ and $C_{\psi,LoS,l}$ in Fig. 4 are given by

$$C_{FF,LoS,l}(\underline{\theta}_{FF}) = \sum_{i=0}^{n_{FF}-1} \theta_{FF}[i] \left(\frac{f_l(z-1)}{z} \right)^{i+1} \quad (21)$$

$$C_{\psi,LoS,l}(\underline{\theta}_{\psi}) = 1 + \sum_{i=0}^{n_{\psi}-1} \theta_{\psi}[i] \left(\frac{f_l(z-1)}{z} \right)^{i+1} \quad (22)$$

with design parameters $\underline{\theta}_{FF}$, $\underline{\theta}_{\psi}$.

Theorem 6 shows that $\underline{\nu}_{FF,LoS,l}$ and $\underline{\rho}_{\psi,LoS,l}$ depend affine on parameters $\underline{\theta}_{FF}$ and $\underline{\theta}_{\psi}$, respectively.

Theorem 6: Given Definition 5, the finite-time descriptions of $\underline{\nu}_{FF,LoS,l}$ and $\underline{\rho}_{\psi,LoS,l}$ are given by

$$\underline{\nu}_{FF,LoS,l} = \underline{C}_{FF,LoS,l} \underline{\mathcal{D}}_F \underline{\psi}_{SS,h} = \underline{\Phi}_{FF,l} \underline{\theta}_{FF} \quad (23)$$

$$\underline{\rho}_{\psi,LoS,l} = \underline{C}_{\psi,LoS,l} \underline{\mathcal{D}}_F \underline{\psi}_{SS,h} = \underline{\mathcal{D}}_F \underline{\psi}_{SS,h} + \underline{\Phi}_{\psi,l} \underline{\theta}_{\psi} \quad (24)$$

with

$$\underline{\Phi}_{x,l} = \underline{\mathcal{D}}_F \underline{T}_{\psi_{SS,h}} \left[\underline{0}_{(N_h-F(n_x+1)) \times (n_x+1)} \right] \underline{R}_{x,l} \quad (25)$$

$$\underline{T}_{\psi_{SS,h}} = \begin{bmatrix} \psi_{SS,h}[0] & 0 & 0 & \cdots & 0 \\ \psi_{SS,h}[1] & \psi_{SS,h}[0] & 0 & \cdots & 0 \\ \psi_{SS,h}[2] & \psi_{SS,h}[1] & \psi_{SS,h}[0] & \cdots & 0 \\ \vdots & \vdots & \vdots & \ddots & \vdots \\ \psi_{SS,h}[N_h-1] & \psi_{SS,h}[N_h-2] & \psi_{SS,h}[N_h-3] & \cdots & \psi_{SS,h}[0] \end{bmatrix} \quad (26)$$

$$\underline{R}_{x,l} = \begin{bmatrix} 1 & 1 & 1 & \cdots & 1 \\ -1 & -2 & -3 & \cdots & -n_x \\ 0 & 1 & 3 & \cdots & * \\ 0 & 0 & -1 & \cdots & * \\ \vdots & \vdots & \vdots & \ddots & \vdots \\ 0 & 0 & 0 & \cdots & (-1)^{n_x} \end{bmatrix} \text{diag} \{f_l^1, \dots, f_l^{n_x}\} \quad (27)$$

where x refers to FF or ψ .

Proof: See Appendix B. \square

Combining Theorem 6 with Lemma 4 reveals an affine dependence of $\underline{\varepsilon}_*$ on $\underline{\theta}_{\text{FF}}$ and $\underline{\theta}_\psi$ as made explicit in Lemma 7.

Lemma 7: Error $\underline{\varepsilon}_*$ is given by

$$\underline{\varepsilon}_* = \underline{b} - \underline{A}\Phi\underline{\theta} \quad (28)$$

with

$$\underline{b} = \underline{\psi}_{\text{SS},*} - \underline{G}_{\text{LoS},*} \underline{H}_{F1} \underline{S}_{\text{LoS},1} \underline{C}_{\text{FB},\text{LoS},1} \underline{D}_F \underline{\psi}_{\text{SS},h} \quad (29)$$

$$\underline{\Phi} = \begin{bmatrix} \underline{\Phi}_{\text{FF},1} & 0 \\ 0 & \underline{\Phi}_{\psi,1} \end{bmatrix} \quad (30)$$

$$\underline{\theta} = \begin{bmatrix} \underline{\theta}_{\text{FF}} \\ \underline{\theta}_\psi \end{bmatrix}. \quad (31)$$

Proof: See Appendix C. \square

Lemma 7 provides the dependence of $\underline{\varepsilon}_*$ on the controller parameters $\underline{\theta}$. In Section IV-B, the parameters $\underline{\theta}$ are optimized.

B. Controller Optimization

The optimal parameters for the control objective in (3) are given by the solution of the optimization problem

$$\min_{\underline{\theta}} \|\underline{\varepsilon}_*\|_2^2 \quad \text{subject to} \quad \underline{\varepsilon}_* = \underline{b} - \underline{A}\Phi\underline{\theta}. \quad (32)$$

If $\underline{A}\Phi$ is full rank, the solution to this quadratic optimization problem is given by the least-squares solution $\underline{\theta} = \underline{\theta}_0$, with

$$\underline{\theta}_0 = ((\underline{A}\Phi)^\top (\underline{A}\Phi))^{-1} (\underline{A}\Phi)^\top \underline{b}. \quad (33)$$

For perfect models, solution (33) provides the optimal solution.

In practice, there are always model mismatches for which the parameters are iteratively learned through an approach that closely resembles norm-optimal ILC [6] based on the models and data of previous executions. A key observation is that the models are time varying, which is in sharp contrast to standard learning techniques. One execution of the learning approach is referred to as a trial or task and indicated with subscript $j = 0, 1, 2, \dots$. The parameters $\underline{\theta}_{j+1}$ for the next trial are determined as those minimizing the performance criterion in Definition 8 [6] based on measured data from trial j .

Definition 8 (Performance Criterion): The performance criterion for trial $j + 1$, $j = 0, 1, 2, \dots$ is given by

$$\mathcal{J}(\underline{\theta}_{j+1}) = \|\underline{\varepsilon}_{j+1,*}\|_{\underline{W}_\varepsilon}^2 + \|\underline{\zeta}_{j+1,l}\|_{\underline{W}_\zeta}^2 + \|\underline{\zeta}_{j+1,l} - \underline{\zeta}_{j,l}\|_{\underline{W}_{\Delta\zeta}}^2 \quad (34)$$

where $\|(\cdot)\|_{\underline{W}}^2 = (\cdot)^\top \underline{W}(\cdot)$, with $\underline{W}_\varepsilon \in \mathbb{R}^{N_* \times N_*}$ positive definite, $\underline{W}_\zeta, \underline{W}_{\Delta\zeta} \in \mathbb{R}^{2N_1 \times 2N_1}$ semipositive definite, and

$$\underline{\varepsilon}_{j+1,*} = \underline{\varepsilon}_{j,*} - \underline{A}\Phi(\underline{\theta}_{j+1} - \underline{\theta}_j) \quad (35)$$

$$\underline{\zeta}_{j+1,l} = \underline{\Phi}\underline{\theta}_j. \quad (36)$$

Performance criterion (34) can be used to address several control goals. For example, for $\underline{W}_\varepsilon = \underline{I}_{N_*}$ and $\underline{W}_\zeta = \underline{W}_{\Delta\zeta} = \underline{0}_{2N_1}$, the control goal in (3) is addressed, i.e., minimizing $\|\underline{\varepsilon}_*\|_2^2$. The optimal parameters for the general criterion are given by Theorem 9.

Theorem 9 (Iterative Solution): The parameters $\underline{\theta}_{j+1}$, $j = 0, 1, 2, \dots$, that minimize $\mathcal{J}(\underline{\theta}_{j+1})$ in Definition 8 are given by

$$\underline{\theta}_{j+1} = \underline{Q}\underline{\theta}_j + \underline{L}\underline{\varepsilon}_{j,*} \quad (37)$$

with

$$\underline{Q} = ((\underline{A}\Phi)^\top \underline{W}_\varepsilon (\underline{A}\Phi) + \underline{\Phi}^\top (\underline{W}_\zeta + \underline{W}_{\Delta\zeta}) \underline{\Phi})^{-1} \times ((\underline{A}\Phi)^\top \underline{W}_\varepsilon (\underline{A}\Phi) + \underline{\Phi}^\top \underline{W}_{\Delta\zeta} \underline{\Phi}), \quad (38)$$

$$\underline{L} = ((\underline{A}\Phi)^\top \underline{W}_\varepsilon (\underline{A}\Phi) + \underline{\Phi}^\top (\underline{W}_\zeta + \underline{W}_{\Delta\zeta}) \underline{\Phi})^{-1} \times (\underline{A}\Phi)^\top \underline{W}_\varepsilon. \quad (39)$$

Theorem 9 directly follows from substitution of (35) and (36) in (34) and equating $\nabla \mathcal{J}(\underline{\theta}_{j+1}) = \underline{0}$ (see also [37]). Note that $\underline{W}_\varepsilon$, \underline{W}_ζ , and $\underline{W}_{\Delta\zeta}$ should be chosen such that the inverse in (38) and (39) exists. A step-by-step procedure for the iterative algorithm is provided in Algorithm 10, where (33) provides initial parameters based on models only.

Algorithm 10 (Iterative Tuning Procedure): Calculate \underline{Q} , \underline{L} using (38), (39), set $j = 0$ and determine $\underline{\theta}_0$ in (33). Then, perform the following sequence of steps.

1. Execute task j and record data $\underline{\varepsilon}_{j,*}$.
2. Determine $\underline{\theta}_{j+1}$ through (37).
3. Set $j \rightarrow j + 1$ and repeat from step 1 until satisfactory convergence in $\underline{\theta}_j$ or a user-defined maximum number of trials is reached.

Algorithm 10 provides the iterative tuning solution for the time-varying multirate system with controller design at the low rate. In Section IV-C, the controllers are explicitly designed and implemented at the high rate to enhance the performance/cost tradeoff in Fig. 1.

C. Performance Enhancement—High-Rate Control

In Section IV-B, the optimal controller for the multirate system in Fig. 4 is presented. In this section, the performance of the multirate system is further improved by modifying the controller implementation and design, which constitutes Contribution (III). The results of Section IV-B are recovered as a special case.

In contrast to time-invariant systems, time-varying systems do not generally commute, i.e., interchanging the order affects the output. One key advantage of the proposed approach is that this property can be directly exploited to enhance the performance/cost tradeoff in Fig. 1. In Fig. 4, both the feedforward controller and input shaper of the long stroke are implemented at the low rate f_l . In this section, these controllers are implemented at high rate f_h as shown in Fig. 5(a). This implementation has the potential to improve the performance since $\psi_{\text{SS},h}$ contains more information than $\rho_{\text{LoS},1} = \mathcal{D}_F \psi_{\text{SS},h}$. This also follows from the noble identity $\mathcal{D}_F H(z^F) \equiv H(z) \mathcal{D}_F$, with H a discrete-time system rational in z [36, Sec. 4.2]. Indeed, since the frequency response of $C_{\text{FF},\text{LoS},h}$ is independent of that of $C_{\text{FF},\text{LoS},1}$, there is more design freedom as illustrated in Fig. 5(b).

The additional cost of the high-rate implementation is negligible since it only involves a different controller design

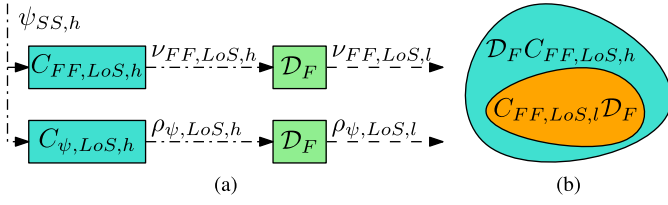


Fig. 5. Designing and implementing the controllers at high rate allow to exploit all information in $\psi_{SS,h}$ and thereby improve performance. (a) Part of the control diagram in Fig. 4 with the controllers implemented at high rate, i.e., $f_c = f_h$. (b) Design space is larger for the controller design at high rate.

in software, without affecting hardware. In particular, it uses sensor information of the short stroke loop at high rate, which is also required for feedback control of the short stroke. The new design does not require sensor information of the long-stroke loop at a higher rate. The actuation of the long-stroke loop remains at low rate.

The parameterization of the controllers at high rate is similar to that in Definition 5 and provided by Definition 11.

Definition 11: $C_{FF,LoS,h}$ and $C_{\psi,LoS,h}$ in Fig. 5 are given by

$$C_{FF,LoS,h}(\theta_{FF}) = \sum_{i=0}^{n_{FF}-1} \theta_{FF}[i] \left(\frac{f_h(z-1)}{z} \right)^{i+1} \quad (40)$$

$$C_{\psi,LoS,h}(\theta_{\psi}) = 1 + \sum_{i=0}^{n_{\psi}-1} \theta_{\psi}[i] \left(\frac{f_h(z-1)}{z} \right)^{i+1}. \quad (41)$$

The finite-time descriptions for this parameterization are provided in Lemma 12. Using these results, the iterative approach outlined in Algorithm 10 is directly applicable.

Lemma 12: Given Definition 11, the finite-time descriptions (23), (24), and (30) change to

$$\underline{\nu}_{FF,LoS,l} = \underline{D}_F \underline{C}_{FF,LoS,h} \underline{\psi}_{SS,h} = \underline{D}_F \underline{\Phi}_{FF,h} \underline{\theta}_{FF} \quad (42)$$

$$\underline{\rho}_{\psi,LoS,l} = \underline{D}_F \underline{C}_{\psi,LoS,h} \underline{\psi}_{SS,h} = \underline{D}_F \underline{\psi}_{SS,h} + \underline{D}_F \underline{\Phi}_{\psi,h} \underline{\theta}_{\psi} \quad (43)$$

$$\underline{\Phi} = \begin{bmatrix} \underline{D}_F \underline{\Phi}_{FF,h} & 0 \\ 0 & \underline{D}_F \underline{\Phi}_{\psi,h} \end{bmatrix} \quad (44)$$

with

$$\underline{\Phi}_{x,h} = \underline{T}_{\psi_{SS,h}} \begin{bmatrix} \underline{I}_{n_x+1} \\ \underline{0}_{(N_h-(n_x+1)) \times (n_x+1)} \end{bmatrix} \underline{R}_{x,h} \quad (45)$$

$$\underline{R}_{x,h} = \begin{bmatrix} 1 & 1 & 1 & \dots & 1 \\ -1 & -2 & -3 & \dots & -n_x \\ 0 & 1 & 3 & \dots & * \\ 0 & 0 & -1 & \dots & * \\ \vdots & \vdots & \vdots & \ddots & \vdots \\ 0 & 0 & 0 & \dots & (-1)^{n_x} \end{bmatrix} \text{diag} \{ f_h^1, \dots, f_h^{n_x} \} \quad (46)$$

where x refers to FF or ψ .

Proof: See Appendix D. \square

The controller design and implementation at high rate complete the multirate controller design. Next, the advantages of multirate control over single-rate control are demonstrated in both simulation and experiments.

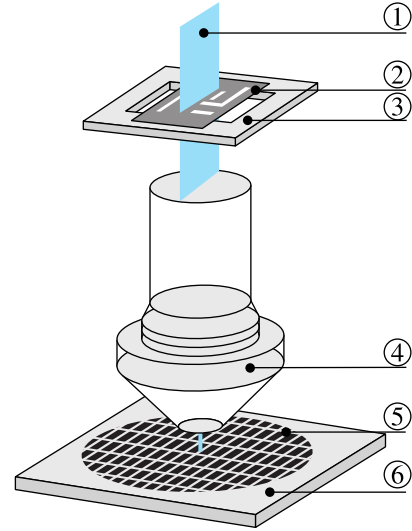


Fig. 6. Schematic of a wafer scanner system, consisting of light source ①, reticle ②, reticle stage ③, lens system ④, wafer ⑤, and wafer stage ⑥.

V. EXPERIMENTAL SETUP—A DUAL-STAGE WAFER STAGE SYSTEM

In the remainder of this paper, the multirate control design framework presented in Section IV is validated on a dual-stage system, both in simulations and experiments. In this section, the wafer stage system is introduced in more detail and the experimental setup of the dual-stage system is presented.

A. Wafer Stages—Key Components in Lithography Machines

Wafer stages are key components in wafer scanners. Wafer scanners are state-of-the-art lithography machines for the automated production of integrated circuits. In Fig. 6, a schematic illustration of a wafer scanner system is depicted. Ultraviolet light from a light source ① passes through a reticle ②, which contains a blueprint of the integrated circuits to be manufactured. The reticle is clamped atop the reticle stage ③, which performs a scanning motion. The resulting image of the reticle is scaled down by a lens system ④ and projected onto the light-sensitive layers of a wafer ⑤. The wafer is clamped on the wafer stage ⑥ and performs a synchronized scanning motion with the reticle stage.

During the scanning process, the wafer stage and reticle stage track reference signals with nanometer positioning accuracy. In this paper, the focus is on the control of the wafer stage, which has more stringent performance requirements than the reticle stage [40].

B. Experimental Setup

The experimental setup is shown in Fig. 7 and consists of two stages: a long stroke (LoS) and a short stroke (SS). Both stages can translate in one horizontal direction and are air guided. Each stage is actuated through a Lorentz actuator attached to the force frame. The position of each stage is measured through 1-nm resolution optical encoders attached to the metrology frame, which is separated from the force frame to reduce interaction. The total stroke is 16.0 mm.

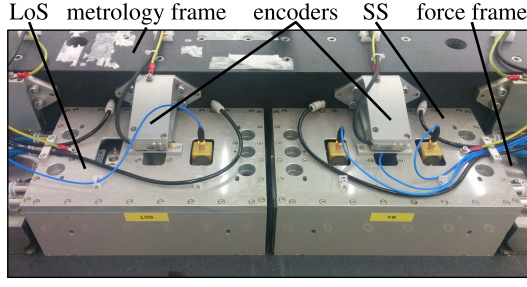


Fig. 7. Experimental setup resembling a one degree-of-freedom wafer stage. The setup consists of two air-guided stages that can translate in one horizontal direction. The positions are measured through 1-nm resolution optical encoders.

The sampling rate of ε_* is $f_* = 10080$ Hz. The identified frequency response functions of both stages are shown in Fig. 8. The stages are modeled as freely moving masses with one sample I/O delay

$$G_{x,*} = z^{-1} \frac{(z+1)}{2m_x f_*^2 (z-1)^2} \quad (47)$$

with masses $m_{SS} = 4.70$ kg and $m_{LoS} = 4.33$ kg. The sampling rate factors F_h, F_l are varied and provided when relevant.

Reference trajectory $\rho_{SS,h}$ consists of a forward and backward movement with a total duration of 0.25 s and is shown in Fig. 9. The point-to-point profile is representative for the application in terms of distance, maximum acceleration, and so on. A fourth-order profile is used to guarantee a smooth signal with limited high-frequency content to avoid excitation of higher order dynamics (see also Fig. 8 and [41]).

Experiments show that the measurement noise on both $\psi_{SS,*}$ and $\psi_{LoS,*}$ has a variance of $(45 \text{ nm})^2$. This value is used during simulation to mimic experimental conditions.

C. Controller Design

The fixed feedback controllers $C_{FB,SS,h}$ and $C_{FB,LoS,l}$ both consist of a lead filter, weak integrator, and second-order lowpass filter based on loop-shaping techniques [5]. The controllers stabilize their respective closed-loop systems and yield a bandwidth (first 0-dB crossing of the open loop) of 100 Hz for both loops. The feedforward controller and input shaper for the short stroke are given by

$$C_{FF,SS,h} = m_{SS} \frac{f_h^2 (z-1)^2}{z^2} \quad (48)$$

$$C_{\psi,SS,h} = G_{SS,h} C_{FF,SS,h}. \quad (49)$$

Hence, $C_{FF,SS,h}$ generates mass feedforward and the combination results in $\underline{g}_{SS,h} = 0$, if $G_{SS,h}$ is exact.

The design of the long-stroke feedforward controller and input shaper aims to minimize $\|\underline{\varepsilon}_*\|_2^2$ by setting the weights in Definition 8 to

$$\underline{W}_{\varepsilon} = \underline{I}_{N_*}, \quad \underline{W}_{\xi}, \underline{W}_{\Delta\xi} = \underline{0}_{2N_1 \times 2N_1}. \quad (50)$$

Note that these settings also facilitate fast convergence of the iterative procedure in Algorithm 10.

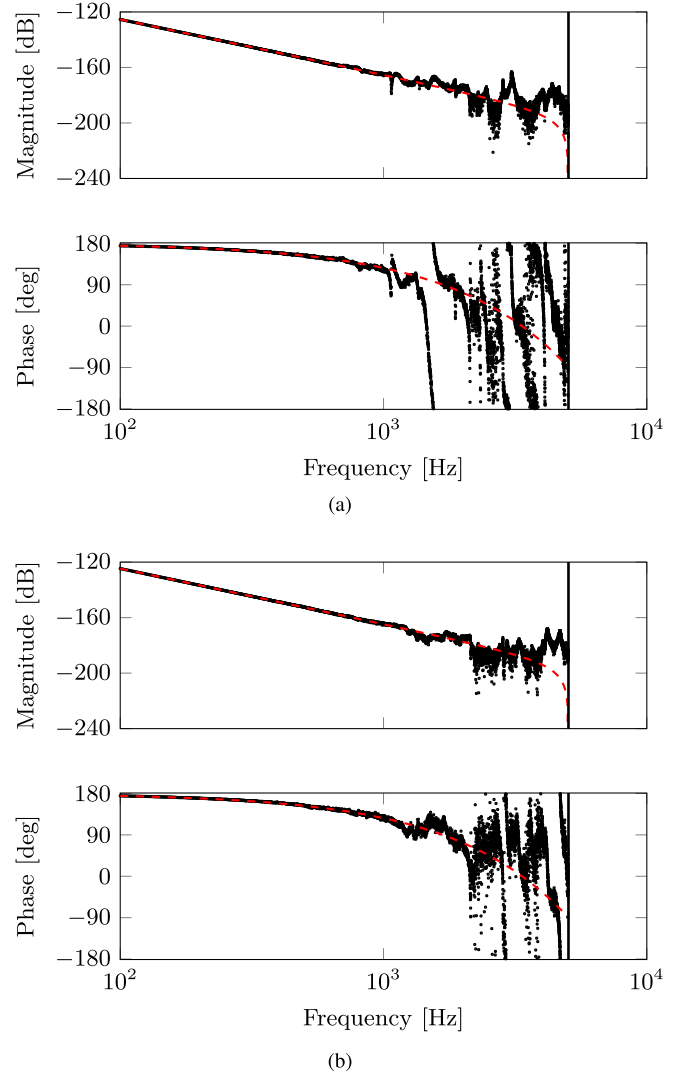


Fig. 8. Measured frequency response functions (●) with sampling rate $f_* = 10080$ Hz and the identified models (---) in (47). (a) SS stage. (b) LoS stage.

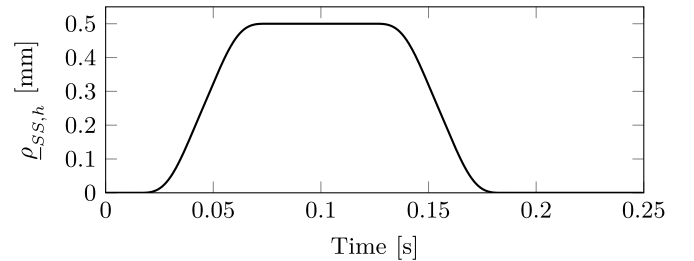


Fig. 9. Reference trajectory $\rho_{SS,h}$ is a forward and backward movement over 0.5 mm constructed from fourth-order polynomials.

VI. SIMULATION RESULTS

In this section, the simulation results are presented, which serve as a benchmark for the experimental results presented in Section VII. The simulations enable validation of the experimental results and constitute Contribution (IV).

A. Comparing Controllers at Different Rates

The considered control configurations are listed in Table I, see also (1). Due to the difference in sampling rate between

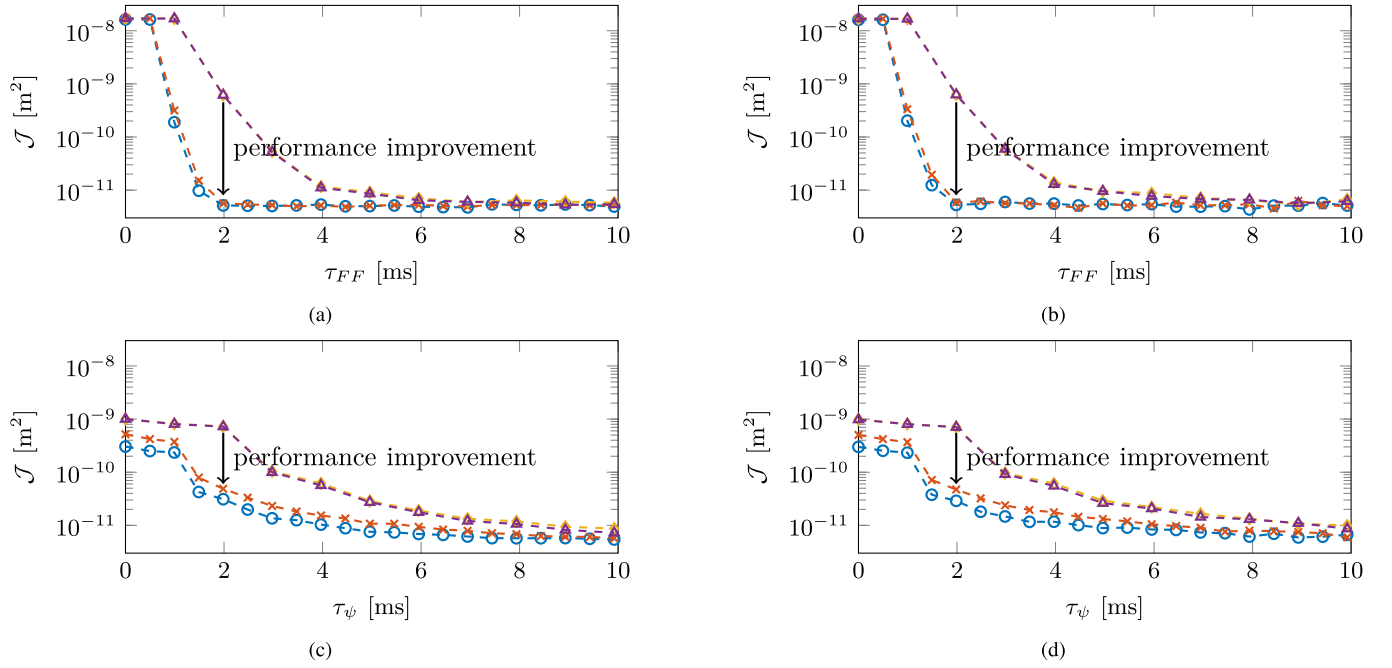


Fig. 10. Simulation results in (a) and (c), and experimental results in (b) and (d) for the four control configurations in Table I. As is expected, single-rate high ($\circ \oplus \cdot$) outperforms single-rate low ($\cdot \blacktriangle \cdot$). The performance of multirate low ($\cdot \blacklozenge \cdot$) is similar to that of single-rate low ($\cdot \blacktriangle \cdot$). The performance of multirate high ($\cdot \times \cdot$) is close to the performance of single-rate high ($\circ \oplus \cdot$). The results demonstrate the advantages of multirate control. Indeed, a high level of performance is achievable with multirate control for limited cost since one of the feedback control loops is evaluated at a lower rate. (a) Simulation results for varying τ_{FF} show that, due to more design freedom in terms of parameters n_{FF} , the performance increases (\mathcal{J} decreases) for increasing cost (increasing buffer length τ_{FF}). The results shown are for fixed $C_{\psi, LoS} = 1$ and varying n_{FF} . (b) Experimental validation of the simulation in (a). The results are in line with the simulation results. (c) Simulation results for varying τ_{ψ} show that larger cost (larger buffer length τ_{ψ}) yields better performance (lower \mathcal{J}). The results shown are for mass feedforward ($n_{FF} = 2$ and $\theta_{FF}[0] = 0$) and varying n_{ψ} . (d) Experimental validation of the simulation in (c). The results are in line with the simulation results.

TABLE I

FOUR DIFFERENT CONTROL CONFIGURATIONS THAT ARE EVALUATED.

Label	Symbol	f_* [Hz]	f_h [Hz]	f_l [Hz]	f_c [Hz]
Single-rate high	$\circ \oplus \cdot$	10080	2016	2016	2016
Single-rate low	$\cdot \blacktriangle \cdot$	10080	1008	1008	1008
Multirate high	$\cdot \times \cdot$	10080	2016	1008	2016
Multirate low	$\cdot \blacklozenge \cdot$	10080	2016	1008	1008

the controller parameterization on low rate (Definition 5) and high rate (Definition 11), the number of parameters n_{FF} and n_{ψ} alone does not provide a fair comparison between the controllers. Therefore, the controller buffer lengths

$$\tau_{FF} := \frac{n_{FF}}{f_c}, \quad \tau_{\psi} := \frac{n_{\psi}}{f_c} \quad (51)$$

are defined, where f_c is the sampling rate of the optimized controllers (see Table I). These buffer lengths are an indication for the implementation cost of the controller.

B. Simulation Setup

For comparison with the experimental results in Section VII, measurement noise is added to $\underline{\psi}_{SS,*}$ and $\underline{\psi}_{LoS,*}$. The noise is modeled as zero mean, Gaussian white noise with variance $\sigma^2 = (45 \text{ nm})^2$ based on experimental data (see also Section V-B).

In the simulation, the models are exact and hence the initial parameters $\underline{\theta}_0$ in (33) provide the optimal solution. Note that

the noise introduces trial-varying disturbances, which cannot be compensated through the iterative tuning algorithm and thereby limits the achievable performance.

C. Results

The performance/cost tradeoff curves for the configurations in Table I are shown in Fig. 10(a) and (c). Both figures show the enhancement of the performance/cost tradeoff through multirate control as illustrated in Fig. 1. In particular, both figures show increasing performance (decreasing \mathcal{J}) for increasing cost (increasing τ) and excellent performance through multirate control with design at high rate.

As a direct consequence of a higher sampling rate, single-rate high outperforms single-rate low. Multirate control is a tradeoff between these two and, hence, the performance is somewhere in between. The performance improvement of multirate low is limited compared to single-rate low. In contrast, the performance of multirate high is close to that of single-rate high. The results show that multirate control can achieve high performance with limited cost when designed and implemented at the high rate. Indeed, the long-stroke feedback control loop remains executed at the low rate.

The results in Fig. 10(a) show the importance of adding the acceleration profile as basis function in terms of performance improvement, as is also apparent from the frequency response functions in Fig. 8 and identified models in (47). Indeed, especially for low frequencies, the stages behave as

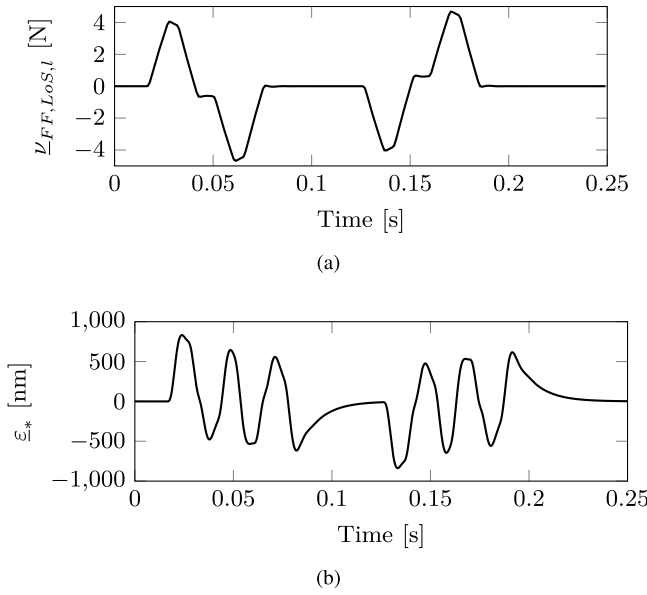


Fig. 11. Time-domain simulation results for single-rate high with $n_{FF} = 2$, $n_{\psi} = 0$. The results show the importance of mass feedforward. (a) Feedforward signal $u_{FF,LoS,l}$. (b) Error signal ϵ_* .

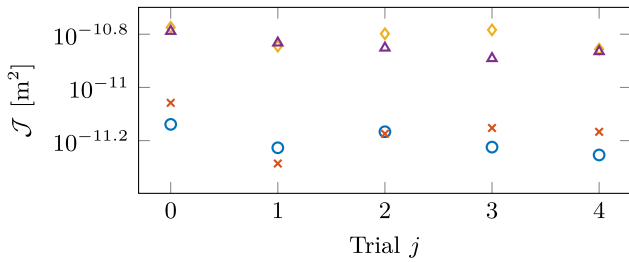


Fig. 12. Experimental results of the performance criterion over trials for $\tau_{FF} = 1$ ms, $\tau_{\psi} = 0$ with single-rate high (○), multirate high (×), multirate low (◇), and single-rate low (△). The results show that all control configurations converge in one trial up to the level of trial-varying disturbances for which the iterative tuning algorithm cannot compensate.

a rigid body mass. Therefore, a mass feedforward controller $C_{FF,LoS} = \theta_{FF}[1](f_c^2(z-1)^2/z^2)$ is used in Fig. 10(c), where parameter $\theta_{FF}[1]$ is also optimized. Note that mass feedforward is also used for the short-stroke feedforward controller in (48).

Time-domain results for multirate high with $n_{FF} = 2$, $n_{\psi} = 0$ are shown in Fig. 11. Compared to mass feedforward, there is an additional parameter in the feedforward filter as can be observed in $u_{FF,LoS,l}$, resulting in improved performance.

The simulation results demonstrate the potential of multirate control, especially when the controllers are designed and implemented at the high rate. Next, the results are experimentally validated.

VII. EXPERIMENTAL RESULTS

In this section, the simulation results of Section VI are experimentally validated on the setup described in Section V. The results experimentally validate the advantages of multirate control and constitute Contribution (V).

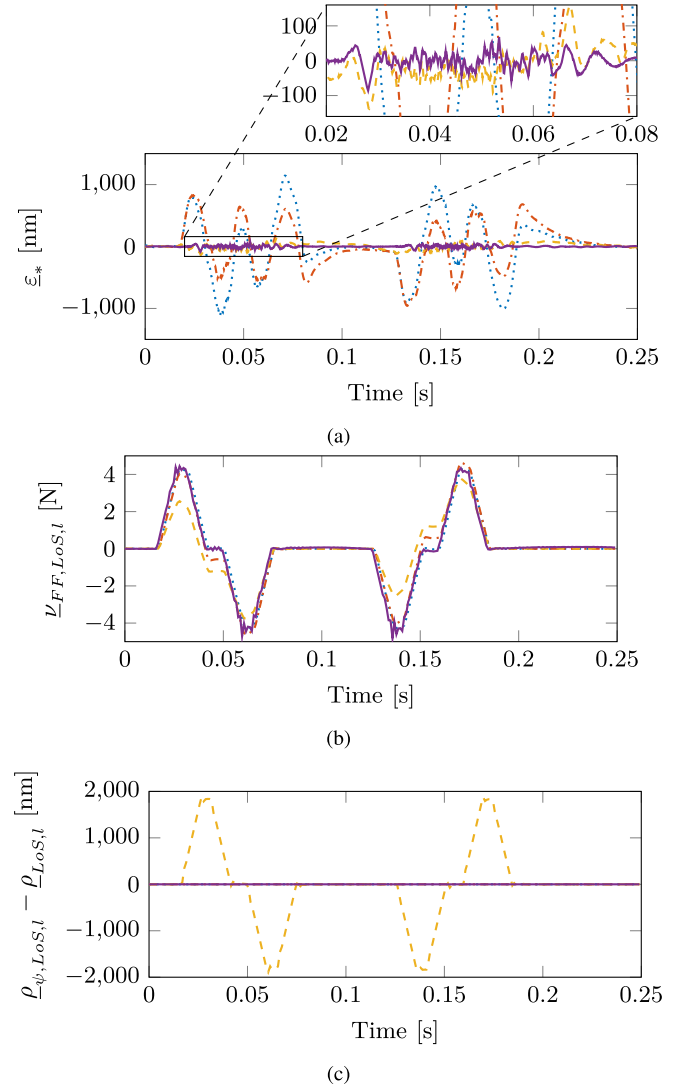


Fig. 13. Time-domain results for multirate high for different parameterizations. In ascending order of design freedom: mass feedforward ($n_{FF} = 2$, $\theta_{FF}[0] = 0$, $n_{\psi} = 0$) (dotted lines); $n_{FF} = 2$, $n_{\psi} = 0$ (dashed-dotted lines); $n_{FF} = 2$, $n_{\psi} = 4$ (dashed lines); and full learning of $u_{FF,LoS,h}$ ($n_{FF} = N_h$, $n_{\psi} = 0$) (solid lines). More design freedom reduces the error ϵ_* . (a) Parameterizations with more design freedom yield a smaller error ϵ_* , which is also apparent in the performance criterion \mathcal{J} shown in Fig. 10. (b) Different parameterizations yield different feedforward signals $u_{FF,LoS,l}$. (c) Shaped input $\rho_{\psi,LoS,l}$ is only different from $\rho_{LoS,l}$ for the parameterization with $n_{\psi} = 4$ (dashed lines) since $n_{\psi} = 0$ for other parameterizations.

A. Application of Iterative Tuning

In contrast to simulation, the models do not exactly describe the system in experiments. Therefore, the iterative tuning procedure in Algorithm 10 is invoked to iteratively update the parameters based on measured data. The convergence of the iterative tuning algorithm is shown in Fig. 12 for the various control configurations in Table I with a fixed buffer length $\tau_{FF} = 1$ ms ($\tau_{\psi} = 0$).

The results in Fig. 12 show fast convergence (one trial) of the iterative algorithm as desired. Note that the deviations over the trials are caused by trial-varying disturbances for which the

algorithm cannot compensate. In the remainder, five trials are used and only the results of the fifth trial are shown.

B. Results

The experimental results for the simulations in Fig. 10(a) and (c) are shown in Fig. 10(b) and (d), respectively. The results are in line with the simulation results and the conclusions in Section VI, i.e., higher performance (lower \mathcal{J}) for increasing number of parameters (increasing τ), and excellent performance for multirate control with control design at high rate (multirate high).

Time-domain signals for several parameterizations with multirate high are shown in Fig. 13. Clearly, mass feedforward only ($n_{FF} = 2$, $\theta_{FF}[0] = 0$, $n_{\psi} = 0$) is restrictive and achieves moderate performance. When using $n_{FF} = 2$, $n_{\psi} = 0$ there is more design freedom resulting in better performance. Adding design freedom in the input shaper by using $n_{FF} = 2$, $n_{\psi} = 4$ yields even better performance. Most design freedom is obtained by fully parameterizing the feedforward signal as in traditional learning control with $n_{FF} = N_h$ ($n_{\psi} = 0$) and yields the best performance. Indeed, the performance of standard learning control in which the full signal is learned is superior for repeating tasks. However, the performance deteriorates drastically when the trajectory $\rho_{SS,h}$ is changed, see [37], [38], which conflicts with the requirement on reference task flexibility in Section II-C. Hence, there is a tradeoff between the performance and the task flexibility, which can be balanced using basis functions.

C. Summary

The experimental results validate the simulation results and, thereby, demonstrate the potential of multirate control for dual-stage systems. Both the simulations and experiments show that a multirate design approach with control design at the high rate can significantly enhance the performance compared to traditional single-rate control on the low rate. In fact, the performance is similar to that of single-rate control at the high rate, but obtained with a lower cost since one of the control loops is executed at the low rate which reduces hardware cost.

VIII. CONCLUSION

In most motion systems, all control loops are operated on a single, fixed sampling rate since this allows the use of well-known control design techniques. However, for such a design, increasing the sampling rate to increase performance is costly in terms of required hardware since all control loops are affected.

In this paper, a multirate approach is exploited to enhance the traditional performance/cost tradeoff. In essence, this allows to allocate the performance and cost over different control loops. The time variance introduced by multirate sampling complicates the control design and constitutes the main challenge addressed in this paper.

The main contribution of this paper is a control design framework for multirate systems. The framework facilitates

the optimal feedforward control design through iterative tuning control. Through simulations and experiments on a dual-stage wafer stage system, the advantages of the multirate control approach are demonstrated. In particular, it is shown that by design of multirate control on the high-rate excellent performance is achieved with limited cost. The results demonstrate the potential of flexible sampling in motion systems.

Ongoing research focuses on the feedback control design for multirate systems, see [26] for preliminary results, and control design for other classes of flexible sampling.

APPENDIX A PROOF LEMMA 4

The following identity, known as the push-through rule, is exploited

$$(\underline{I}_m + \underline{A}\underline{B})^{-1}\underline{A} = \underline{A}(\underline{I}_n + \underline{B}\underline{A})^{-1} \quad (52)$$

with $\underline{A} \in \mathbb{R}^{m \times n}$, $\underline{B} \in \mathbb{R}^{n \times m}$, $n, m \in \mathbb{N}$.

Using Fig. 4 and (52), $\underline{\psi}_{SS,*}$ is expressed in $\rho_{SS,h}$

$$\underline{\psi}_{SS,*} = \underline{G}_{SS,*} \underline{H}_{F_h} (\underline{C}_{FF,SS,h} + \underline{C}_{FB,SS,h} \underline{C}_{\psi,SS,h}) \rho_{SS,h} - \underline{G}_{SS,*} \underline{H}_{F_h} \underline{C}_{FB,SS,h} \underline{D}_{F_h} \underline{\psi}_{SS,*} \quad (53)$$

$$= (\underline{I}_{N_*} + \underline{G}_{SS,*} \underline{H}_{F_h} \underline{C}_{FB,SS,h} \underline{D}_{F_h})^{-1} \underline{G}_{SS,*} \underline{H}_{F_h} \times (\underline{C}_{FF,SS,h} + \underline{C}_{FB,SS,h} \underline{C}_{\psi,SS,h}) \rho_{SS,h} \quad (54)$$

$$= \underline{G}_{SS,*} \underline{H}_{F_h} (\underline{I}_{N_h} + \underline{C}_{FB,SS,h} \underline{D}_{F_h} \underline{G}_{SS,*} \underline{H}_{F_h})^{-1} \times (\underline{C}_{FF,SS,h} + \underline{C}_{FB,SS,h} \underline{C}_{\psi,SS,h}) \rho_{SS,h} \quad (55)$$

$$= \underline{G}_{SS,*} \underline{H}_{F_h} \underline{S}_{SS,h} \times (\underline{C}_{FF,SS,h} + \underline{C}_{FB,SS,h} \underline{C}_{\psi,SS,h}) \rho_{SS,h} \quad (56)$$

with $\underline{S}_{SS,h}$ in (19). Using Fig. 4 and (52), $\underline{\psi}_{LoS,*}$ is expressed in $\rho_{\psi,LoS,l}$, $\underline{\psi}_{FF,LoS,l}$

$$\underline{\psi}_{LoS,*} = \underline{G}_{LoS,*} \underline{H}_{F_l} (\underline{V}_{FF,LoS,l} + \underline{C}_{FB,LoS,l} \underline{D}_{F_l} \underline{\psi}_{LoS,*}) - \underline{G}_{LoS,*} \underline{H}_{F_l} \underline{C}_{FB,LoS,l} \underline{D}_{F_l} \underline{\psi}_{LoS,*} \quad (57)$$

$$= (\underline{I}_{N_*} + \underline{G}_{LoS,*} \underline{H}_{F_l} \underline{C}_{FB,LoS,l} \underline{D}_{F_l})^{-1} \underline{G}_{LoS,*} \underline{H}_{F_l} \times (\underline{V}_{FF,LoS,l} + \underline{C}_{FB,LoS,l} \underline{D}_{F_l} \underline{\psi}_{LoS,*}) \quad (58)$$

$$= \underline{G}_{LoS,*} \underline{H}_{F_l} (\underline{I}_{N_l} + \underline{C}_{FB,LoS,l} \underline{D}_{F_l} \underline{G}_{LoS,*} \underline{H}_{F_l})^{-1} \times (\underline{V}_{FF,LoS,l} + \underline{C}_{FB,LoS,l} \underline{D}_{F_l} \underline{\psi}_{LoS,*}) \quad (59)$$

$$= \underline{G}_{LoS,*} \underline{H}_{F_l} \underline{S}_{LoS,l} \times [\underline{I}_{N_l} \underline{C}_{FB,LoS,l}] \begin{bmatrix} \underline{V}_{FF,LoS,l} \\ \underline{\rho}_{\psi,LoS,l} \end{bmatrix} \quad (60)$$

$$= \underline{A} \begin{bmatrix} \underline{V}_{FF,LoS,l} \\ \underline{\rho}_{\psi,LoS,l} \end{bmatrix} \quad (61)$$

with $\underline{S}_{LoS,l}$ in (20) and \underline{A} in (18). The result follows from $\underline{\varepsilon}_* = \underline{\psi}_{SS,*} - \underline{\psi}_{LoS,*}$.

APPENDIX B PROOF THEOREM 6

It is shown that for the parameterization

$$C_1(\theta) = \sum_{i=0}^{n-1} \theta[i] \left(\frac{f_1(z-1)}{z} \right)^{i+1} \quad (62)$$

it holds

$$\underline{\xi}_1 = \underline{C}_1 \underline{D}_F \underline{\rho}_{SS,h} = \underline{\Phi}_1 \underline{\theta}. \quad (63)$$

Relations (23) and (24) directly follow from this result.

Parameterization (62) can equivalently be written as a finite impulse response (FIR) structure of order $n_\alpha = n + 1$

$$C_1(\theta) = \sum_{i=0}^{n-1} \theta[i] \left(\frac{f_1(z-1)}{z} \right)^{i+1} = \sum_{i=0}^{n_\alpha-1} \alpha[i] z^{-i}. \quad (64)$$

By equating coefficients, it directly follows that the relation between the parameters is given by $\underline{\alpha} = \underline{R}_1 \underline{\theta}$ with $\underline{R}_1 \in \mathbb{R}^{n_\alpha \times n}$ as given in (27). Note that \underline{R}_1 is the product of a truncated transposed (lower triangular Cholesky factor of the) Pascal matrix of order n_α , with a diagonal scaling matrix depending on f_1 .

The finite-time description of C_1 in terms of $\underline{\alpha}$ is given by

$$\underline{C}_1 = \begin{bmatrix} \alpha[0] & 0 & 0 & \cdots \\ \alpha[1] & \alpha[0] & 0 & \cdots \\ \vdots & \alpha[1] & \alpha[0] & \cdots \\ \alpha[n_\alpha - 1] & \vdots & \alpha[1] & \ddots \\ 0 & \alpha[n_\alpha - 1] & \vdots & \ddots \\ 0 & 0 & \alpha[n_\alpha - 1] & \ddots \\ \vdots & \vdots & \vdots & \ddots \end{bmatrix}. \quad (65)$$

Using the Kronecker mixed-product property rule (14), the order of \underline{C}_1 and \underline{D}_F , see (10), is interchanged

$$\underline{C}_1 \underline{D}_F = (\underline{C}_1 \otimes 1) (\underline{I}_{N_1} \otimes \underline{e}_F^\top) \quad (66)$$

$$= (\underline{C}_1 \underline{I}_{N_1}) \otimes (1 \underline{e}_F^\top) \quad (67)$$

$$= (\underline{I}_{N_1} \underline{C}_1) \otimes ((\underline{e}_F^\top \underline{e}_F) \underline{e}_F^\top) \quad (68)$$

$$= (\underline{I}_{N_1} \otimes \underline{e}_F^\top) (\underline{C}_1 \otimes (\underline{e}_F \underline{e}_F^\top)) \quad (69)$$

$$= \underline{D}_F (\underline{C}_1 \otimes (\underline{e}_F \underline{e}_F^\top)). \quad (70)$$

Note that $\underline{C}_1 \otimes (\underline{e}_F \underline{e}_F^\top)$ is a lower triangular matrix and that $\underline{\psi}_{SS,h} = \underline{T}_{\psi_{SS,h}} \underline{e}_{N_h}$, with $\underline{T}_{\psi_{SS,h}}$ in (26) is also a lower triangular matrix.

Next, the commutative property of lower triangular matrices is exploited to express $\underline{\xi}_1$ in $\underline{\theta}$. To this end, the Kronecker product rule and the relation $\underline{\alpha} = \underline{R}_1 \underline{\theta}$ are used

$$\underline{\xi}_1 = \underline{C}_1 \underline{D}_F \underline{\psi}_{SS,h} \quad (71)$$

$$= \underline{D}_F (\underline{C}_1 \otimes (\underline{e}_F \underline{e}_F^\top)) \underline{\psi}_{SS,h} \quad (72)$$

$$= \underline{D}_F (\underline{C}_1 \otimes (\underline{e}_F \underline{e}_F^\top)) \underline{T}_{\psi_{SS,h}} \underline{e}_{N_h} \quad (73)$$

$$= \underline{D}_F \underline{T}_{\psi_{SS,h}} (\underline{C}_1 \otimes (\underline{e}_F \underline{e}_F^\top)) \underline{e}_{N_h} \quad (74)$$

$$= \underline{D}_F \underline{T}_{\psi_{SS,h}} \begin{bmatrix} \underline{\alpha} \otimes \underline{e}_F \\ \underline{0}_{(N_h - F n_\alpha) \times 1} \end{bmatrix} \quad (75)$$

$$= \underline{D}_F \underline{T}_{\psi_{SS,h}} \begin{bmatrix} (\underline{I}_{n_\alpha} \underline{\alpha}) \otimes (\underline{e}_F 1) \\ \underline{0}_{(N_h - F n_\alpha) \times 1} \end{bmatrix} \quad (76)$$

$$= \underline{D}_F \underline{T}_{\psi_{SS,h}} \begin{bmatrix} \underline{I}_{n_\alpha} \otimes \underline{e}_F \\ \underline{0}_{(N_h - F n_\alpha) \times n_\alpha} \end{bmatrix} \underline{\alpha} \quad (77)$$

$$= \underline{D}_F \underline{T}_{\psi_{SS,h}} \begin{bmatrix} \underline{I}_{n_\alpha} \otimes \underline{e}_F \\ \underline{0}_{(N_h - F n_\alpha) \times n_\alpha} \end{bmatrix} \underline{R}_1 \underline{\theta} \quad (78)$$

$$= \underline{\Phi}_1 \underline{\theta} \quad (79)$$

which concludes the proof of (62). Relations (23) and (24) directly follow from this result.

APPENDIX C PROOF LEMMA 7

Substitution of (23) and (24) in (16) and using (18) yields

$$\underline{\varepsilon}_* = \underline{\psi}_{SS,*} - \underline{A} \begin{bmatrix} \underline{v}_{FF,LoS,l} \\ \underline{\rho}_{\psi,LoS,l} \end{bmatrix} \quad (80)$$

$$= \underline{\psi}_{SS,*} - \underline{A} \begin{bmatrix} \underline{\Phi}_{FF,l} \underline{\theta}_{FF} \\ \underline{D}_F \underline{\psi}_{SS,h} + \underline{\Phi}_{\psi,l} \underline{\theta}_{\psi} \end{bmatrix} \quad (81)$$

$$= \underline{\psi}_{SS,*} - \underline{A} \begin{bmatrix} \underline{0}_{N_l} \\ \underline{D}_F \underline{\psi}_{SS,h} \end{bmatrix} - \underline{A} \begin{bmatrix} \underline{\Phi}_{FF,l} \underline{\theta}_{FF} \\ \underline{\Phi}_{\psi,l} \underline{\theta}_{\psi} \end{bmatrix} \quad (82)$$

$$= \underline{\psi}_{SS,*} - \underline{G}_{LoS,*} \underline{H}_{F_l} \underline{S}_{LoS,l} [\underline{I}_{N_l} \underline{C}_{FB,LoS,l}] \times \begin{bmatrix} \underline{0}_{N_l} \\ \underline{D}_F \underline{\psi}_{SS,h} \end{bmatrix} - \underline{A} \begin{bmatrix} \underline{\Phi}_{FF,l} \underline{\theta}_{FF} \\ \underline{\Phi}_{\psi,l} \underline{\theta}_{\psi} \end{bmatrix} \quad (83)$$

$$= \underline{\psi}_{SS,*} - \underline{G}_{LoS,*} \underline{H}_{F_l} \underline{S}_{LoS,l} \underline{C}_{FB,LoS,l} \underline{D}_F \underline{\psi}_{SS,h} - \underline{A} \begin{bmatrix} \underline{\Phi}_{FF,l} & 0 \\ 0 & \underline{\Phi}_{\psi,l} \end{bmatrix} \begin{bmatrix} \underline{\theta}_{FF} \\ \underline{\theta}_{\psi} \end{bmatrix} \quad (84)$$

$$= \underline{b} - \underline{A} \underline{\Phi} \underline{\theta} \quad (85)$$

with \underline{b} , $\underline{\Phi}$, $\underline{\theta}$ as given in Lemma 7.

APPENDIX D PROOF LEMMA 12

It is shown that for the general parameterization

$$C_h(\theta) = \sum_{i=0}^{n-1} \theta[i] \left(\frac{f_h(z-1)}{z} \right)^{i+1} \quad (86)$$

it holds

$$\underline{\xi}_1 = \underline{D}_F \underline{C}_h \underline{\psi}_{SS,h} = \underline{D}_F \underline{\Phi}_h \underline{\theta}. \quad (87)$$

Relations (42) and (43) directly follow from this result.

The proof is similar to that of Theorem 6. First, C_h is expressed in terms of FIR parameters $\underline{\alpha}$

$$C_h(\theta) = \sum_{i=0}^{n-1} \theta[i] \left(\frac{f_h(z-1)}{z} \right)^{i+1} = \sum_{i=0}^{n_\alpha-1} \alpha[i] z^{-i} \quad (88)$$

where $\underline{\alpha} = \underline{R}_h \underline{\theta}$ with $\underline{R}_h \in \mathbb{R}^{n_\alpha \times n}$ as given in (46) and $n_\alpha = n + 1$. The finite-time description of C_h in terms of $\underline{\alpha}$ is given by

$$\underline{C}_h = \begin{bmatrix} \alpha[0] & 0 & 0 & \cdots \\ \alpha[1] & \alpha[0] & 0 & \cdots \\ \vdots & \alpha[1] & \alpha[0] & \cdots \\ \alpha[n_\alpha - 1] & \vdots & \alpha[1] & \ddots \\ 0 & \alpha[n_\alpha - 1] & \vdots & \ddots \\ 0 & 0 & \alpha[n_\alpha - 1] & \ddots \\ \vdots & \vdots & \vdots & \ddots \end{bmatrix}. \quad (89)$$

Next, it is exploited that the lower triangular matrices \underline{C}_h and $\underline{T}_{\psi_{SS,h}}$ commute

$$\underline{\xi}_1 = \underline{D}_F \underline{C}_h \underline{\psi}_{SS,h} \quad (90)$$

$$= \underline{D}_F \underline{C}_h \underline{T}_{\psi_{SS,h}} \underline{e}_{N_h} \quad (91)$$

$$= \underline{D}_F \underline{T}_{\psi_{SS,h}} \underline{C}_h \underline{e}_{N_h} \quad (92)$$

$$= \underline{D}_F \underline{T}_{\psi_{SS,h}} \begin{bmatrix} \underline{a} \\ \underline{0}_{(N_h-n_a) \times 1} \end{bmatrix} \quad (93)$$

$$= \underline{D}_F \underline{T}_{\psi_{SS,h}} \begin{bmatrix} \underline{I}_{n_a} \\ \underline{0}_{(N_h-n_a) \times n_a} \end{bmatrix} \underline{a} \quad (94)$$

$$= \underline{D}_F \underline{T}_{\psi_{SS,h}} \begin{bmatrix} \underline{I}_{n_a} \\ \underline{0}_{(N_h-n_a) \times n_a} \end{bmatrix} \underline{R}_h \underline{\theta} \quad (95)$$

$$= \underline{D}_F \underline{\Phi}_h \underline{\theta}. \quad (96)$$

Relations (42) and (43) directly follow from this result.

ACKNOWLEDGMENT

The authors would like to thank G. Leenknegt for his contributions to the experimental setup.

REFERENCES

- [1] T. Chen and B. A. Francis, *Optimal Sampled-Data Control Systems*. London, U.K.: Springer, 1995.
- [2] K. J. Åström and B. Wittenmark, *Computer Control System Theory Design*, 3rd ed. Englewood Cliffs, NJ, USA: Prentice-Hall, 1997.
- [3] S. Skogestad and I. Postlethwaite, *Multivariable Feedback Control: Analysis and Design*, 2nd ed. Hoboken, NJ, USA: Wiley, Nov. 2005.
- [4] G. F. Franklin, J. D. Powell, and A. Emami-Naeini, *Feedback Control of Dynamic Systems*, 7th ed. Upper Saddle River, NJ, USA: Pearson, 2015.
- [5] M. Steinbuch, R. J. E. Merry, M. L. G. Boerlage, M. J. C. Ronde, and M. J. G. van de Molengraft, "Advanced motion control design," in *The Control Handbook: Control System Applications*, 2nd ed., W. S. Levine, Ed. Boca Raton, FL, USA: CRC Press, 2010.
- [6] D. A. Bristow, M. Tharayil, and A. G. Alleyne, "A survey of iterative learning control," *IEEE Control Syst. Mag.*, vol. 26, no. 3, pp. 96–114, Jun. 2006.
- [7] D. P. Glasson, "Development and applications of multirate digital control," *IEEE Control Syst. Mag.*, vol. CSM-3, no. 4, pp. 2–8, Nov. 1983.
- [8] J. Salt and M. Tomizuka, "Hard disk drive control by model based dual-rate controller. Computation saving by interlacing," *Mechatronics*, vol. 24, no. 6, pp. 691–700, 2014.
- [9] J. Salt and P. Albertos, "Model-based multirate controllers design," *IEEE Trans. Control Syst. Technol.*, vol. 13, no. 6, pp. 988–997, Nov. 2005.
- [10] S. Lall and G. Dullerud, "An LMI solution to the robust synthesis problem for multi-rate sampled-data systems," *Automatica*, vol. 37, no. 12, pp. 1909–1922, Dec. 2001.
- [11] W. Ohnishi, T. Beauduin, and H. Fujimoto, "Preactuated multirate feedforward for a high-precision stage with continuous time unstable zeros," *IFAC-PapersOnLine*, vol. 50, no. 1, pp. 10907–10912, 2017.
- [12] X. Chen and H. Xiao, "Multirate forward-model disturbance observer for feedback regulation beyond Nyquist frequency," *Syst. Control Lett.*, vol. 94, pp. 181–188, Aug. 2016.
- [13] J. Ding, F. Marcassa, S.-C. Wu, and M. Tomizuka, "Multirate control for computation saving," *IEEE Trans. Control Syst. Technol.*, vol. 14, no. 1, pp. 165–169, Jan. 2006.
- [14] S.-H. Lee, "Multirate digital control system design and its application to computer disk drives," *IEEE Trans. Control Syst. Technol.*, vol. 14, no. 1, pp. 124–133, Jan. 2006.
- [15] H. Fujimoto, Y. Hori, and A. Kawamura, "Perfect tracking control based on multirate feedforward control with generalized sampling periods," *IEEE Trans. Ind. Electron.*, vol. 48, no. 3, pp. 636–644, Jan. 2001.
- [16] D. Antunes and W. P. M. H. Heemels, "Frequency-domain analysis of control loops with intermittent data losses," *IEEE Trans. Autom. Control*, vol. 61, no. 8, pp. 2295–2300, Aug. 2016.
- [17] T. Oomen and C. R. Rojas, "Sparse iterative learning control with application to a wafer stage: Achieving performance, resource efficiency, and task flexibility," *Mechatronics*, vol. 47, pp. 134–147, Nov. 2017.
- [18] J. Valencia, E. P. van Horssen, D. Goswami, W. P. M. H. Heemels, and K. Goossens, "Resource utilization and Quality-of-Control trade-off for a composable platform," in *Proc. Des. Autom. Test Europe Conf. Exhibit. (DATE)*, Dresden, Germany, Mar. 2016, pp. 654–659.
- [19] J. van Zundert, T. Oomen, D. Goswami, and W. P. M. H. Heemels, "On the potential of lifted domain feedforward controllers with a periodic sampling sequence," in *Proc. Amer. Control Conf.*, Boston, Massachusetts, Jul. 2016, pp. 4227–4232.
- [20] S. Fraser, M. Attia, and M. Osman, "Modelling, identification and control of thermal deformation of machine tool structures, part 1: Concept of generalized modelling," *J. Manuf. Sci. Eng.*, vol. 120, no. 3, pp. 623–631, Aug. 1999.
- [21] A. Aminifar, E. Bini, P. Eles, and Z. Peng, "Analysis and design of real-time servers for control applications," *IEEE Trans. Comput.*, vol. 65, no. 3, pp. 834–846, Mar. 2016.
- [22] O. Lindgarde and B. Lennartson, "Performance and robust frequency response for multirate sample-data systems," in *Proc. Amer. Control Conf.*, Albuquerque, NM, USA, Jun. 1997, pp. 3877–3881.
- [23] M. W. Cantoni and K. Glover, "Frequency-domain analysis of linear periodic operators with application to sampled-data control design," in *Proc. 36th IEEE Conf. Decision Control*, San Diego, CA, USA, Dec. 1997, pp. 4318–4323.
- [24] H. Sandberg, E. Mollerstedt, and B. Bernhardsson, "Frequency-domain analysis of linear time-periodic systems," *IEEE Trans. Autom. Control*, vol. 50, no. 12, pp. 1971–1983, Dec. 2005.
- [25] T. Oomen, M. van de Wal, and O. Bosgra, "Design framework for high-performance optimal sampled-data control with application to a wafer stage," *Int. J. Control*, vol. 80, no. 6, pp. 919–934, Jan. 2007.
- [26] J. van Zundert and T. Oomen, "LPTV loop-shaping with application to non-equidistantly sampled precision mechatronics," in *Proc. IEEE 15th Int. Workshop Adv. Motion Control*, Tokyo, Japan, Mar. 2018, pp. 467–472.
- [27] T. Oomen, J. van de Wijdeven, and O. Bosgra, "Suppressing intersample behavior in iterative learning control," *Automatica*, vol. 45, no. 4, pp. 981–988, Apr. 2009.
- [28] R. M. Schmidt, G. Schitter, and J. van Eijk, *The Design of High Performance Mechatronics*. Amsterdam, The Netherlands: Delft Univ. Press, 2011.
- [29] J. C. D. van Zundert, J. L. C. Verhaegh, W. H. T. M. Aangenent, T. Oomen, D. Antunes, and W. P. M. H. Heemels, "Feedforward for multi-rate motion control: Enhanced performance and cost-effectiveness," in *Proc. Amer. Control Conf.*, Chicago, IL, USA, Jul. 2015, pp. 2831–2836.
- [30] B. Bamieh, J. B. Pearson, B. A. Francis, and A. Tannenbaum, "A lifting technique for linear periodic systems with applications to sampled-data control," *Syst. Control Lett.*, vol. 17, no. 2, pp. 79–88, Aug. 1991.
- [31] M. van de Wal, G. van Baars, F. Sperling, and O. Bosgra, "Multivariable H_∞/μ feedback control design for high-precision wafer stage motion," *Control Eng. Pract.*, vol. 10, no. 7, pp. 739–755, Jul. 2002.
- [32] M. F. Heertjes, B. van der Velden, and T. Oomen, "Constrained iterative feedback tuning for robust control of a wafer stage system," *IEEE Trans. Control Syst. Technol.*, vol. 24, no. 1, pp. 56–66, Jan. 2016.
- [33] H. Butler, "Adaptive feedforward for a wafer stage in a lithographic tool," *IEEE Trans. Control Syst. Technol.*, vol. 21, no. 3, pp. 875–881, May 2013.
- [34] M. G. Wassink, M. van de Wal, C. Scherer, and O. Bosgra, "LPV control for a wafer stage: Beyond the theoretical solution," *Control Eng. Pract.*, vol. 13, no. 2, pp. 231–245, Feb. 2005.
- [35] H. Butler, "Position control in lithographic equipment: An enabler for current-day chip manufacturing," *IEEE Control Syst. Mag.*, vol. 31, no. 5, pp. 28–47, Oct. 2011.
- [36] P. P. Vaidyanathan, *Multirate Systems and Filter Banks*. Upper Saddle River, NJ, USA: Prentice-Hall, 1993.
- [37] J. Bolder, T. Oomen, S. Koekebakker, and M. Steinbuch, "Using iterative learning control with basis functions to compensate medium deformation in a wide-format inkjet printer," *Mechatronics*, vol. 24, no. 8, pp. 944–953, Dec. 2014.
- [38] J. Bolder and T. Oomen, "Rational basis functions in iterative learning control—With experimental verification on a motion system," *IEEE Trans. Control Syst. Technol.*, vol. 23, no. 2, pp. 722–729, Mar. 2015.
- [39] F. Boeren, D. Bruijnen, N. van Dijk, and T. Oomen, "Joint input shaping and feedforward for point-to-point motion: Automated tuning for an industrial nanopositioning system," *Mechatronics*, vol. 24, no. 6, pp. 572–581, Sep. 2014.

- [40] E. Evers, M. van de Wal, and T. Oomen, "Synchronizing decentralized control loops for overall performance enhancement: A Youla framework applied to a wafer scanner," *IFAC-PapersOnLine*, vol. 50, no. 1, pp. 10845–10850, Jul. 2017.
- [41] P. Lambrechts, M. Boerlage, and M. Steinbuch, "Trajectory planning and feedforward design for electromechanical motion systems," *Control Eng. Pract.*, vol. 13, no. 2, pp. 145–157, Feb. 2005.



Jurgen van Zundert received the M.Sc. degree (Hons.) in mechanical engineering from the Eindhoven University of Technology, Eindhoven, The Netherlands, in 2014, where he is currently pursuing the Ph.D. degree with the Control Systems Technology Group, Department of Mechanical Engineering. His current research interests include feedforward motion control, multirate control, and iterative learning control.



Tom Oomen (SM'06) received the M.Sc. degree (*cum laude*) and the Ph.D. degree from the Eindhoven University of Technology (TU/e), Eindhoven, The Netherlands.

He held visiting positions at KTH Royal Institute of Technology, Stockholm, Sweden, and The University of Newcastle, Newcastle, NSW, Australia. He is currently an Associate Professor with the Department of Mechanical Engineering, TU/e. His current research interests include system identification, robust control, and learning control, with applications in mechatronic systems.

Dr. Oomen was a recipient of the Corus Young Talent Graduation Award, the 2015 IEEE Transactions on Control Systems Technology Outstanding Paper Award, and the 2017 IFAC Mechatronics Best Paper Award. He is an Associate Editor of the IEEE CONTROL SYSTEMS LETTERS and *IFAC Mechatronics*.



Jan Verhaegh received the M.Sc. degree (Hons.) in mechanical engineering from the Eindhoven University of Technology, Eindhoven, The Netherlands.

Since 2015, he has been a Research Scientist with the Department of Integrated Vehicle Safety, TNO, Helmond, The Netherlands. His current research interests include vehicle dynamics and (wireless) control topics related to automated and cooperative driving technologies. He is involved in projects include design of Robust and Fail-Safe Cooperative Adaptive Cruise Control in truck platooning and the

development, and implementation of Active Lane Keep Assist for high-way automation.



Wouter Aangenent received the M.Sc. degree (*cum laude*) and the Ph.D. degree in mechanical engineering from the Eindhoven University of Technology, Eindhoven, The Netherlands, in 2004 and 2008, respectively.

In 2008, he joined the Research Department of ASML, Veldhoven, The Netherlands, where he currently leads the Mechatronics and Control Research Group.



Duarte J. Antunes (M'13) was born in Viseu, Portugal, in 1982. He received the Licenciatura in electrical and computer engineering from the Instituto Superior Técnico (IST), Lisbon, Portugal, in 2005, and the Ph.D. degree in automatic control with the Institute for Systems and Robotics, IST, in 2011.

From 2011 to 2013, he held a postdoctoral position at the Eindhoven University of Technology (TU/e). He is currently an Assistant Professor with the Department of Mechanical Engineering, TU/e. His current research interests include networked control systems, stochastic control, dynamic programming, and systems biology.



W. P. M. H. Heemels (F'16) received the M.Sc. degree (*summa cum laude*) in mathematics and the Ph.D. degree (*summa cum laude*) in control theory from the Eindhoven University of Technology (TU/e), Eindhoven, The Netherlands, in 1995 and 1999, respectively.

From 2000 to 2004, he was with the Electrical Engineering Department, TU/e. From 2004 to 2006, he was with the Embedded Systems Institute, Eindhoven. Since 2006, he has been with the Department of Mechanical Engineering, TU/e, where he is currently a Full Professor. He held visiting professor positions at the Swiss Federal Institute of Technology, Zürich, Switzerland, in 2001, and the University of California at Santa Barbara, Santa Barbara, CA, USA, in 2008. He was with Océ, Venlo, The Netherlands, in 2004. His current research interests include hybrid and cyber-physical systems, networked and event-triggered control systems, and constrained systems including model predictive control.

Dr. Heemels was a recipient of a personal VICI grant awarded by STW (Dutch Technology Foundation). He served/serves on the Editorial Boards for *Automatica*, *Nonlinear Analysis: Hybrid Systems*, *Annual Reviews in Control*, and the IEEE TRANSACTIONS ON AUTOMATIC CONTROL.